COBEM 2023 27TH INTERNATIONAL CONGRESS OF MECHANICAL ENGENEERING

ABCM Brazilian Society of Mechanical Sciences and Engineering
27th ABCM International Congress of Mechanical Engineering
December 04-08, 2023, Florianópolis-SC, Brazil

COB-2023-1051
NUMERICAL ANALYSIS OF ENDPLATE DRAG COMPONENTS FOR A LOW SPEED AIRCRAFT

Breno Lopes Tumelero
Filipe Dutra da Silva
TEG-Thermofluids Engineering Group, Universidade Federal de Santa Catarina, Joinville, SC, Brazil
breno.tumelero@teg.ufsc.br
filipe.dutra@teg.ufsc.br

Rafael Gigena Cuenca
Universidade Federal de Santa Catarina, Joinville, SC, Brazil
rafael.cuenca@ufsc.br

Abstract. *A greater efficiency in terms of fuel consumption and performance is a recurring target in aeronautical research. In this context, one way to achieve this goal is through drag reduction, allowing an increase in the aerodynamic efficiency of the airplanes, reducing its operation costs and greenhouse gasses emissions. On low flight speeds, most of the total drag is due to induced drag component, as consequence of the high lift coefficient, which increases the downwash along the wing span. One solution to reduce that downwash is the attachment of endplates at the wingtips, which are plates, parallel to the plane's longitudinal axis, working as a barrier that reduces airflow from the lower surface of the wing to the upper. However, depending on the geometry, dimensions and flight conditions, the parasite and interference drag created by the endplate, can reduce the overall benefits of the device. Therefore, this study aims to evaluate, by using computational fluid dynamics tools, the main drag components in different shapes of endplates. Reynolds-averaged Navier Stokes simulations were conducted using the K-ω SST turbulence model, alongside several sensitivity tests, including domain size, grid refinement and turbulence model and parameters. For the validation, the numerical results are compared to experimental wind tunnel results available in the literature for an AR 4 Wortmann FX 63-137 wing, at a Reynolds number of 100000. Thereafter, a parametric analysis was performed in which different sizes of endplates were simulated. The induced and parasite drag components were separated, aiming to discuss the contribution of each drag component to the total drag for each analyzed geometry. Results show an induced drag factor reduction of up to 13.35%, and also that although the parasite drag created by the endplate may reduce its efficiency in some cases, moderate sized geometries can reduce the overall parasite drag on the wing by moving the wingtip vortex away from the surface. Bigger plates were preferred for higher angles of attack, due to its induced drag reduction, while smaller ones proved to be viable choices for cruise flight conditions, avoiding excessive parasite drag increase.*

Keywords: *Endplates, Unmanned aerial vehicle, Induced drag reduction, CFD Simulation using OpenFoam.*

1. INTRODUCTION

With the aeronautical industry focus on greater efficiency in the past few decades, research related to drag reduction in aircraft have a major importance, not only during preliminary project developments, but also for final optimization processes. According to McCormick (1995), for low Mach flows, aircraft drag can be separated in two main components: the induced and the parasite drag. The influence of each component changes according to the flight phase.

The first component is directly related to the lift generation, and is created by the circulation distribution along the wing span. This produces a pressure difference between the upper and lower wing surface, causing the air to flow around the wingtip. This changes the wing effective angle of attack α, which causes the resulting force to have a component pointing backwards, the so-called induced drag D_i (Anderson, 2010).

On the other hand, the second component includes all the additional drag sources, such as the pressure and the skin friction drag. For a subsonic streamlined body, the skin friction drag is responsible for almost the totality of parasite drag and is caused by the shear stresses on the wetted surface area (Raymer, 2018).

In this context, among the main available methods for drag reduction, wingtip devices stand out for effectively reducing the induced drag, having usage in various aircraft types. If not correctly sized, the wet area increase created by the device may reduce the cruise aerodynamic efficiency, as it has a direct influence on the parasite drag (Maughmer, 2006). For this reason, evaluating each drag component contribution to the total drag is crucial for an efficient project.

This paper aims to assess the influence of endplates as wingtip devices. The geometries are modeled according to Roberts (1966) method, which uses the wing airfoil isobars to shape the endplate geometry. Furthermore, the induced

drag is computed using the Trefftz-plane analysis, based on the momentum integral equation and depending mainly on the transversal kinetic energy of the flow (Cummings *et al.*, 1996; Monsch *et al.*, 2007).

To achieve this, numerical simulations of an AR 4 Wortmann FX 63-137 wing, operating at a Reynolds number of 10×10^5, were performed using the OpenFOAM open source CFD software. The wing model has a 0.5m chord, which resulted in a freestream velocity of 3m/s.

2. METHOD

2.1 Computation of Induced Drag

Two different analytical methods were compared for the induced drag coefficient estimation ($CD_i = \frac{D_i}{q.S}$), with q being the dynamic pressure and S the reference wing area. In both of them, CD_i can be calculated through Equation 1, where CL is lift coefficient, AR is the wing aspect ratio and e is the Oswald span efficiency factor.

$$CD_i = \frac{CL^2}{\pi e AR} \tag{1}$$

The first one, explained by McCormick (1995), uses the Lifting Line Theory (LLT) to numerically compute a value δ, for wings with different AR and taper ratio values. This way, e can be computed using Equation 2, using a δ value of 0.025 for the given wing geometry.

$$e = \frac{1}{1+\delta} \tag{2}$$

On the other hand, the second one, proposed by Raymer (2018), uses an empirical estimation, based on real data from straight aircraft wings. The Oswald coefficient is then calculated using Equation 3.

$$e = 1.78(1 - 0.045AR^{0.68}) - 0.64 \tag{3}$$

To compare the theoretical values with the numerical CD_i, the Trefftz plane method was used. Also known as the far field calculation, it is an integral form of the momentum equation, assuming steady-state flow, with no body forces acting on the wing and considering only the higher order terms. More theoretical details about the formulation from the momentum equation to the final form (Equation 4) are explained by Monsch *et al.* (2007) and Cummings *et al.* (1996). Such approach extracts data from a plane far downstream S_T and perpendicular to the freestream flow to calculate the induced drag generated by the wing. The required data can be obtained from the flow field computed through CFD.

$$D_i = \frac{1}{2}\rho_\infty \int\int_{S_T} (v^2 + w^2) dydz \tag{4}$$

According to Bourdin (2002), in CFD simulations involving lifting flow, the transversal kinetic energy decays as it moves away from the wing, at a much faster rate than in reality. This phenomenon happens due to numerical dissipation, which effect is more expressive in far field, as the computational grid tends to become coarser in this region.

As a way to attenuate this problem, Van der Vooren and Slooff (1994) proposed the use of a near field correction to the classic Trefftz plane approach, reinserting terms to the integral that have been previously neglected by the classic model. Thus, the plane can be placed closer to the wing trailing edge, where the mesh is finer and the artificial dissipation is less expressive. The induced drag generated by the wing can be then calculated through the integral shown in Equation 5.

$$D_i = \frac{1}{2}\rho_\infty \int\int_{S_T} (v^2 + w^2) - (1 - M_\infty^2)\Delta u^2 dydz \tag{5}$$

Finally, comparing the theoretical values for the base wing CD_i with the results obtained from the plane integration allows a calibration, through the ratio between these values. Such analysis was also performed by Monsch *et al.* (2007), evaluating the influence of mesh density and plane distance (from the trailing edge) on the CD_i resulted from the plane integration. Moreover, this comparison can be used as a correction for the drag calculated for different endplate models, as a way to keep it closer to an expected theoretical value by using the ratio $CD_{i(trefftz)}/CD_{i(theoretical)}$ taken from the base wing.

2.2 Simulation model

For the simulations, incompressible Reynolds-Averaged Navier-Stokes (RANS) simulations were performed using the k-ω SST turbulence model and the SIMPLE algorithm for solving the pressure-velocity coupling. The second order linear upwind scheme was chosen for the velocity advective term, as tests showed better convergence with reduced numerical diffusion, while the also second order limited linear was used for the remaining variables. Furthermore, for the gradient terms, the multi-directional cell-limited was used for velocity with a limiting factor of 0.5. For the remaining variables, the cell-limited scheme was chosen.

A hexahedral shaped computational domain was adopted, with a symmetry plane in one of the sides (wing root), an outlet condition at downstream boundary and a freestream condition in the remaining faces, as shown in Figure 1. The domain had height and length of 100 times the wing chord, and width of 10 times the wing semispan. Both the domain geometry and the computational mesh were created using SALOME 9.7.

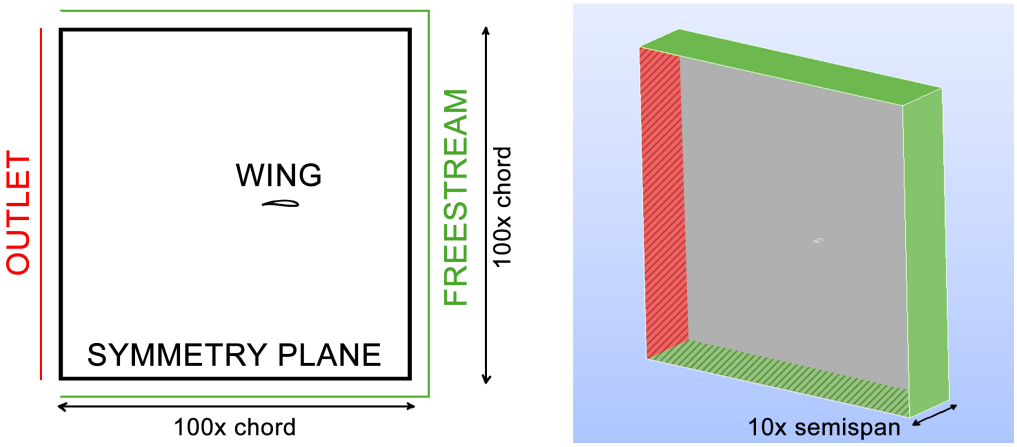

Figure 1. Computational domain.

The mesh was mainly composed by tetrahedrons, with layers of prismatic cells adjacent to the wing surface, in order to discretize the boundary layer. As initial meshing tests showed problems with elongated elements near the trailing edge, and a high cell count due to the leading edge refinement with the standard NETGEN 2D method, a surface structuring was developed on the wing.

For this, each edge was individually discretized, allowing a surface mapping to be executed, and the resulting quadrangles were then splitted into triangles to avoid pyramid type elements right after the prismatic layer, which are incompatible with the mesh export file extension.It is important to mention that this mapping required adding a small radius to the trailing edge, that was also discretized and mapped, allowing the prismatic layer elements to have a near constant size in this region.

Following the method proposed by Roberts (1966), the endplate geometries were modeled following the Wortmann FX 63-137 airfoil isobars, obtained by a CFD simulation of the wing, at an angle of attack of 10°. This approach is capable of providing an optimized geometry, minimizing the induced drag for the same endplate size, when compared to a square-shaped endplate, for example (Tumelero *et al.*, 2021).

The geometries were parameterized by its chord length ratio, and three different geometries were evaluated (Figure 2), corresponding to the matching isobar that intersects the airfoil line at 30, 50 and 70% of the total chord length. Here, the endplate lateral area corresponds to the area within the isobar, but excluding the airfoil itself, exemplified also in Figure 2 for the 70% endplate as the red colored region.

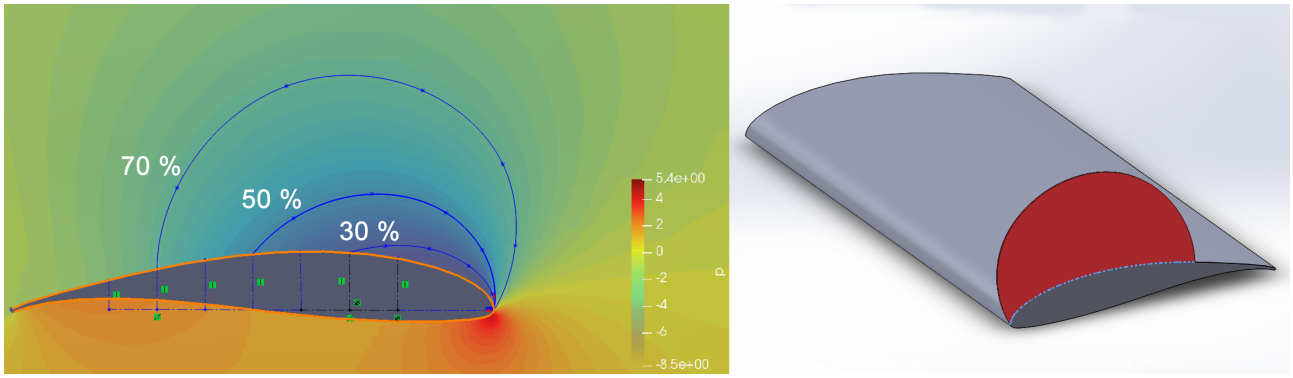

Figure 2. Endplate geometries.

Aiming to ensure the reliability and accuracy of the results from the CFD model, tests performed on a previously published study evaluated the influence of the domain size and turbulence model (Tumelero *et al.*, 2022), working as a base for the simulation model used in the present study.

As a way to assure the results are not impaired by the computational grid refinement, a sensibility test was performed using the Grid Convergence Index method, described by Roache (1997) and Celik *et al.* (2008). This method shows how close the results are to achieving a asymptotic value, where an increase in the grid refinement, no longer affect the results.

Using a minimum recommended refine ratio of 1.3, as shown in Equation 6, where N is the total cell count and X_i is the cell volume, starting from a intermediate mesh (2), two additional meshes can be generated: a finer (1) and a coarser (3). Then, the lift and drag coefficients are taken as the interest variables ϕ for the analysis. Using the difference between their values in each mesh $\epsilon_{12} = \phi_1 - \phi_2$, the method apparent order can be calculated through Equation 8.

$$r = \frac{h_{coarse}}{h_{fine}} \tag{6}$$

$$h = \left[\frac{1}{N}\sum_{i=1}^{N} X_i\right]^{1/3} \tag{7}$$

$$p = \frac{1}{ln(r)} ln\left|\epsilon_{12}/\epsilon_{23}\right| \tag{8}$$

After the calculations above, the asymptotic extrapolated values from the finer mesh, the relative error and the extrapolated relative error can be calculated using Equations 9 to 11.

$$\phi_{ext}^{23} = \frac{(r_{23})^p \phi_3 - \phi_2}{(r_{23})^p - 1} \tag{9}$$

$$e_a^{23} = \frac{\phi_3 - \phi_2}{\phi_3} \tag{10}$$

$$e_{ext}^{23} = \frac{\phi_{ext}^{23} - \phi_3}{\phi_{ext}^{23}} \tag{11}$$

Finally, the GCI index, which shows how close the results are to achieving a point where increasing the grid refinement will no longer affect the obtained values, is calculated using a safety factor of 1.25 (12), resulting in a reliability of 95% (Wilcox, 2006).

$$GCI = \frac{1.25 e_a}{(r^p) - 1} \tag{12}$$

After that, numerical values were compared to experimental wind tunnel tests, performed by Abtahi (1985), Ananda *et al.* (2012) and Bastedo and Mueller (1986). Finally, the three modeled endplates were simulated at an angle of attack α of 10 and 0 degrees, to assess its impact on both high CL and cruise flight conditions.

The k-ω SST turbulence model was used for the simulations. The inlet values for the turbulence variables were defined according to the recommendations made by Spalart and Rumsey (2007), from which k and ω can be calculated through Equations 13 to 14.

$$k = 1 \times 10^{-6} U_\infty^2 \tag{13}$$

$$\omega = \frac{5 U_\infty}{c} \tag{14}$$

Also, more widely used parameters such as the turbulent intensity I and the viscosity ratio $\frac{\mu_t}{\mu}$, can be obtained using the Equations 15 and 16. For this study, the recommended values for the turbulence variables resulted in a turbulent intensity of 0,08165% and a viscosity ratio of 0,02.

$$I = \frac{\sqrt{\frac{2}{3}k}}{U_\infty} \tag{15}$$

$$\frac{\mu_t}{\mu} = \frac{k}{\nu\omega} \tag{16}$$

The induce drag was computed, based on the CFD results, using Equation 5 with the integration function of the software Paraview. Then, the obtained values were compared to both analytical approaches previously mentioned, for each downstream position of the Trefftz plane. In this way, it was possible to calibrate the expected numerical results through the ratio $CD_i(numerical)/CD_i(theoretical)$ (R), shown in Equation 17, calculated for all the tested α range.

$$CD_i = R\, CD_{i(numerical)} \tag{17}$$

So, the induced drag computed from the wings with endplates are divided by this ratio R, as a way to correct the numerical error and estimate a real induced drag coefficient based on the analytical approaches. Table 1 lists the drag components evaluated and how each of them could be obtained.

Table 1. Drag components and its calculation method.

Component	Method
Total drag CD	surface forces integration
Induced drag CD_i	Trefftz plane + correction (R)
Endplate total drag $CD_{endplate}$	Surface forces integration
Total parasite drag $CD_{p(tot)}$	$CD - CD_i$
Wing parasite drag CD_p	$CD - CD_i - CD_{endplate}$
Wing skin friction drag CD_f	Surface shear stress integration
Endplate skin friction drag $CD_{f(endplate)}$	Surface shear stress integration

3. RESULTS

Values seen in Table 2, corresponding to the GCI test results, show that the coefficients from the intermediate mesh are satisfactorily close to both the finer mesh and the extrapolated values, with a maximum error of around 1%, even with two times more mesh cells. Also, as $GCI_{23} < GCI_{12}$, a reduction on the mesh refinement influence can be assessed, therefore, refining the mesh more did not showed up as an advantageous option, mainly due to the small GCI change and the computational cost increase.

Table 2. GCI test results.

Variable	Description	Value
e_a^{23} (CL)	Approximate relative error CL	0.2442%
e_a^{23} (CD)	Approximate relative error CD	0.8038%
e_{ext}^{23} (CL)	Extrapolated relative error CL	0.1551%
e_{ext}^{23} (CD)	Extrapolated relative error CD	0.2812%
e_{ext2}^{23} (CL)	Relative error, extrapolated from the intermediate mesh CL	0.3997%
e_{ext2}^{23} (CD)	Relative error, extrapolated from the intermediate mesh CD	1.0873%
GCI_{23} (CL)	GCI between meshes 2 and 3 CL	0.1936%
GCI_{23} (CD)	GCI between meshes 2 and 3 CD	0.3505%
GCI_{2ext} (CL)	GCI between mesh 2 and the extrapolated result CL	0.3169%
GCI_{2ext} (CD)	GCI between mesh 2 and the extrapolated result CD	0.4742%

In sequence, the numerical results were compared to experimental data available in the literature, as shown in Figures 3 and 4. It is possible to notice the considerable difference between the experimental data, what can be related to the method and construction quality of the wing model, or different wind tunnel test section sizes, for example. For the lift coefficient, the k-ω SST predicted the stall quite close to the Abtahi (1985) and Bastedo and Mueller (1986). As for the drag coefficient, it was capable of performing satisfactorily well, with similar values to all the experimental data, with the main difference being the stall behavior.

Regarding the Trefftz plane, the integration depends mainly on the v and w velocity components, more expressive on the wingtip vortex region. Two additional mesh testes were made, first refining the vortex region, and then increasing the mesh refinement globally with the same refinement ratio of 1.3 used during the GCI tests, except for the wing surface. To evaluate this, the ratio $CD_i(numerical)/CD_i(theoretical)$ was analyzed for each mesh, according to the Trefftz plane distance downstream after the wing trailing edge. It is possible to notice in Figure 5 the artificial dissipation problem on the base mesh, which was highly reduced after refining the vortex region. The global refinement also improved the results, and near the wing trailing edge the CD_i values start to no longer be influenced by the plane distance. Due to the mesh cell count increase from 1356347 to 6786147 elements, no further tests were made, and the distance of one chord behind the trailing edge was chosen for the Trefftz plane placement, to avoid any undesirable influence from the wing wake. With this positioning, the ratio value, designated as R, was set as 0.8508 for the LLT method, and 0.8149 for Raymer method.

After defining the mesh for the Trefftz plane integration, the simulations containing the wing+endplates sets could be performed. Results presented in Figure 6 showed a nearly linear variation of the CL increase with the endplate lateral area, whereas the CD shows an initial increase in drag, and then a considerable reduction for geometries with 50 and 70% chord length. This increase in the total drag may be related to the endplate parasite drag addition, together with the plate being too small to effectively block the vortex in these conditions.

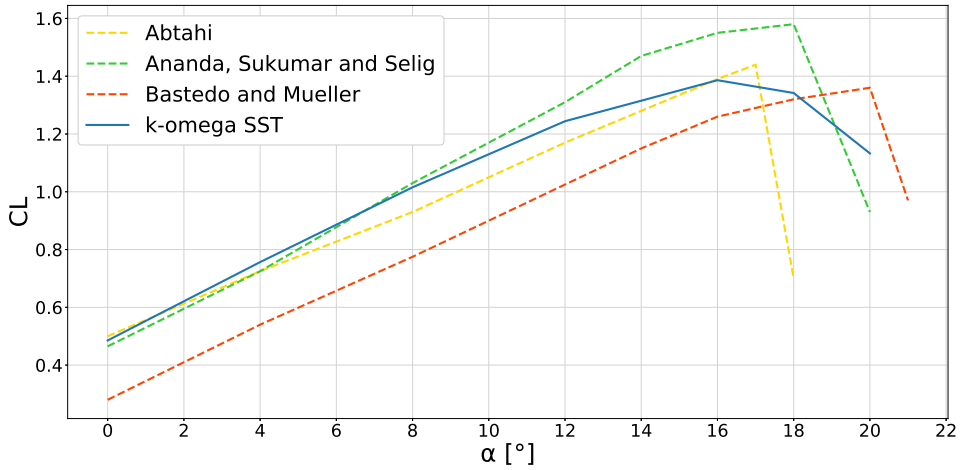

Figure 3. Numerical vs experimental comparison (CL).

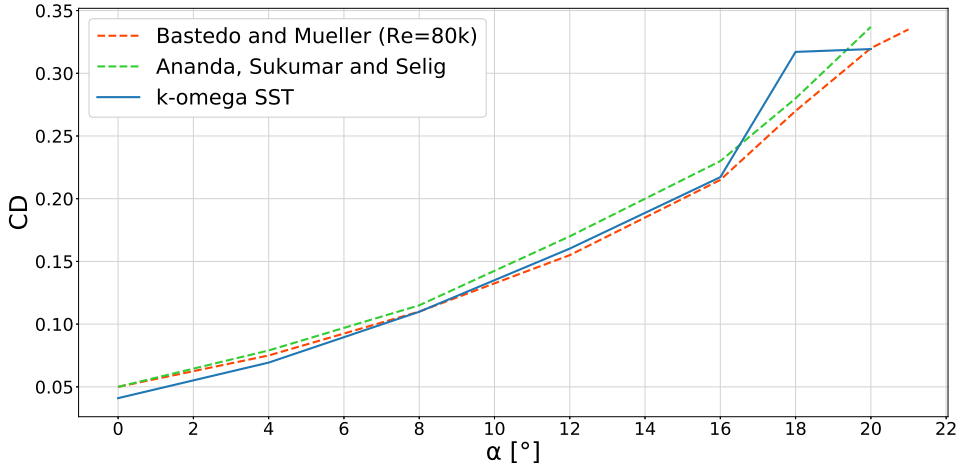

Figure 4. Numerical vs experimental comparison (CD).

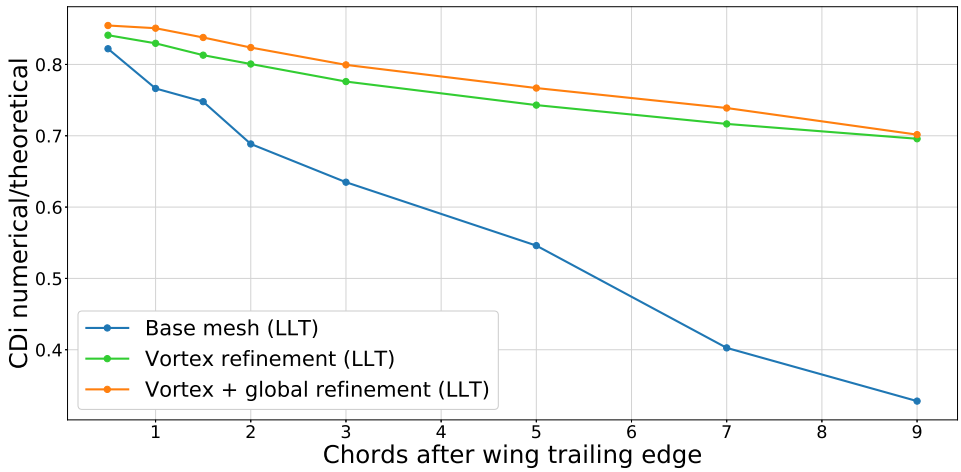

Figure 5. CDi numerical/theoretical for each Trefftz plane positioning.

It is important to mention that the linear behavior for the increase in CL has a limit, as the pressure around the wing profile tends to equal the freestream pressure at a sufficient distance from the surface, reducing the endplate effect as its size increases. Due to this, the L/D ratio will also decrease at some point, as the drag created by the endplate addition proportionally surpasses the CL increase. For this paper, the wing low aspect ratio may have favored larger plates, as the induced drag has a larger contribution on the total drag when compared to higher AR wings.

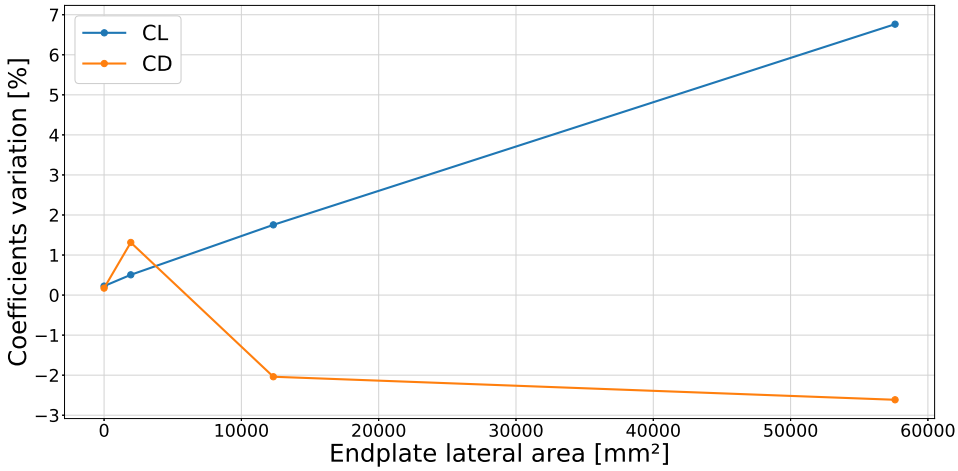

Figure 6. CL and CD variation with endplate size.

Following the same trend as the lift coefficient, the induced drag factor K also had a near-linear variation as the plate size increased (Figure 7). Again, note that these results can be affected by the usage of the ratio R during the plane calibration process, and also by the plane integration itself, mainly due to the artificial dissipation. On the other hand, the overall aerodynamic efficiency was reduced by less than 1% for the 30% chord length geometry, but was followed by an increase of around 4% for the second plate, and a maximum of 9.63% for the largest tested endplate, as shown in Figure 7.

This sudden increase in efficiency from the first to the second geometry shows that the 50% plate is able to effectively reduce the induced drag, while causing no significant addition to the parasite drag. As for the last geometry, the reduction in the L/D curve indicates that the total drag caused by the endplate starts to impair the device efficiency, apart from reducing the K by almost 14%.

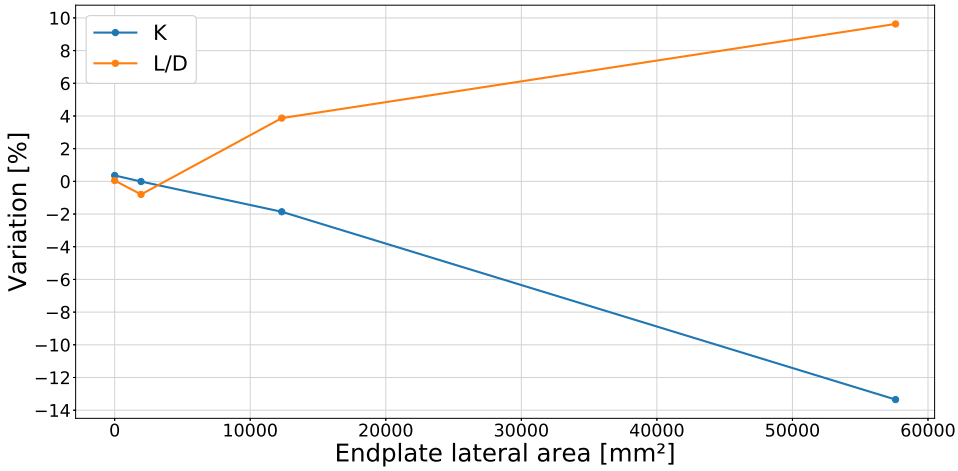

Figure 7. K and L/D variation with endplate size.

The induced drag coefficient CD_i, evaluated using both theoretical approaches (LLT and Raymer) for the calibration process to obtain the ratio R, is shown in Figure 8. Excepting for the third geometry, all the other ones actually increased the total CD_i, as the CL increase also creates mode induced drag for a small K reduction. As this reduction increases for almost 12% from the second to the third plate, the 70% endplate managed to reduce the induced drag, even with the larger lift coefficient.

However, the parasite drag coefficient CD_p analysis presented in Figure 9 shows that the addition of the endplates to the wings actually reduced the total CD_p for the two larger geometries, even if the plates alone increased this drag component. When further studying this effect, it was found that the wingtip vortex created a low pressure zone at the region, increasing both the pressure and the skin friction drag. Adding the endplates reduced this effect, resulting in a smaller total CD_p.

The endplate simulations were then performed again at an α of 0°, to compare the endplate effects in both high lift and cruise conditions, with adjusted R values being 0.8531 for the LLT and 0.8171 for Raymer. It is possible to notice that even if the K reduction was close to the values from α=10°, the L/D increase was much smaller, rounding at about 2% for the smaller plate (Figure 10).

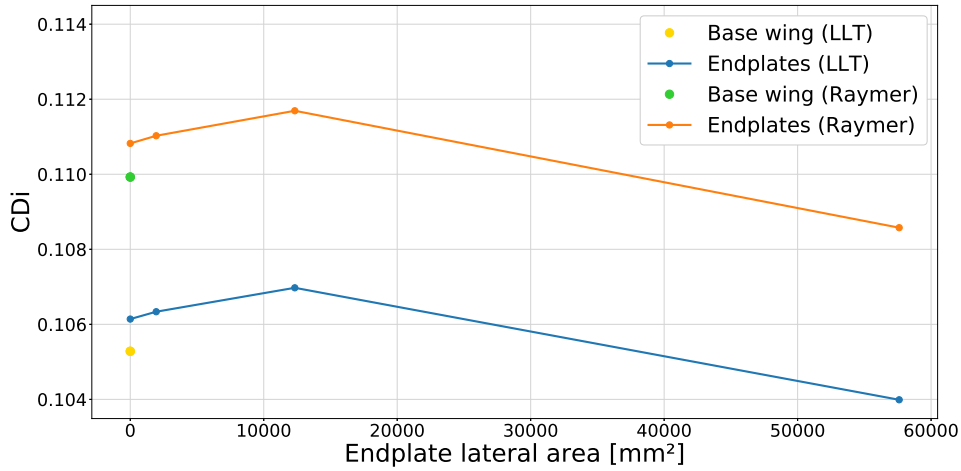

Figure 8. CD_i variation with endplate size.

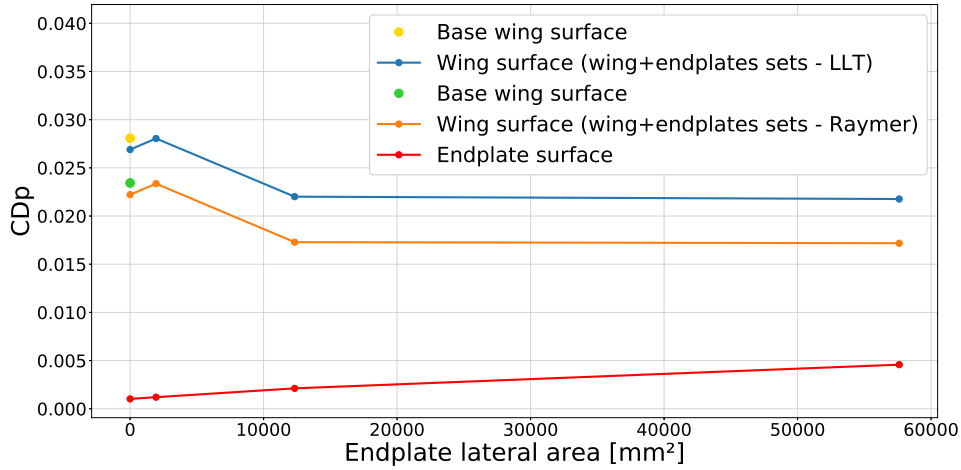

Figure 9. Parasite drag coefficient variation with endplate size.

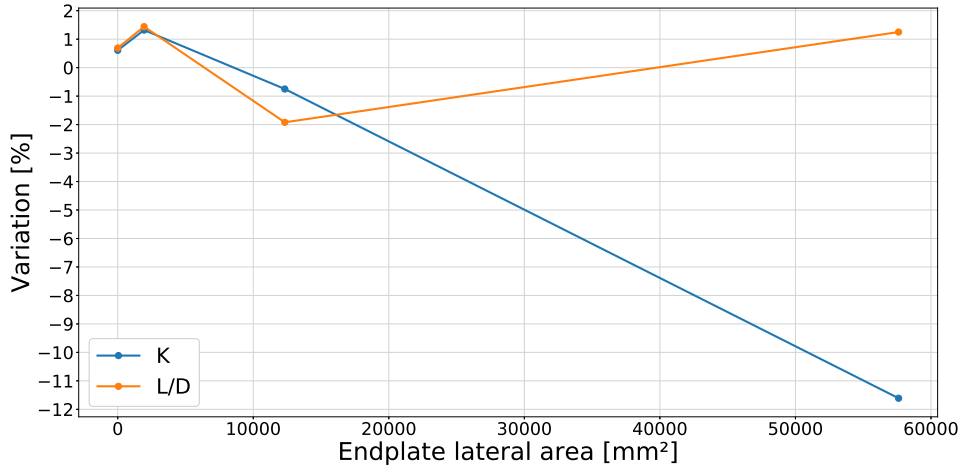

Figure 10. K and L/D variation with endplate size (α=0°).

This change is mainly related to the smaller induced drag influence in the wing total drag, and also by the reduction of the parasite drag increase created by the wingtip vortex. So, adding the endplates slightly reduced the CD_i, while increasing the CD_p even more, as can be seen in Figure 11.

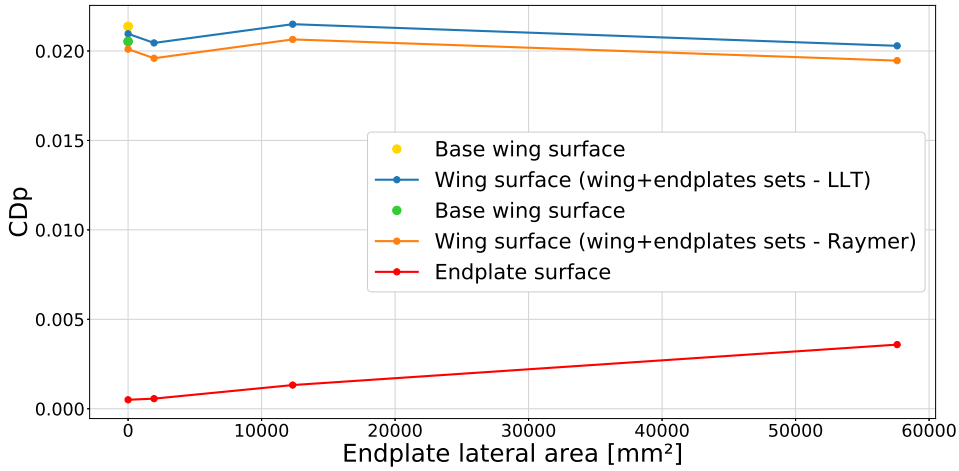

Figure 11. Parasite drag coefficient variation with endplate size (α=0°).

4. CONCLUSIONS

The present work developed a CFD model for aerodynamic evaluation of aircraft wings, with the capability of extracting the induced drag. The computational mesh, turbulence model and variables were be set aiming to maximize the model's accuracy together with a reduced computational cost.

For the induced drag analysis, the artificial dissipation problem could be mitigated by adding a mesh refinement at the wingtip vortex area, which showed great improvement over the results when compared to theoretical values.

According to the Trefftz plane analysis, the endplates addition showed up as a great way to increase the aerodynamic efficiency at higher α values, reaching a maximum of 9.63%, but failed to keep these values at lower CL conditions. This way, the device usage is still limited at cruise flight, as the parasite drag caused by its addition can be greater than the induced drag reduction caused by it. In the end, the elevated induced drag contribution on the wing total drag at high angles of attack favored the bigger geometry, whereas smaller ones came up as a viable choice for lower angles.

For future studies, the maximum lift coefficient increase caused by the endplates addition could be analyzed, as well as the addition of a wider Reynolds range for better representing cruise conditions.

5. REFERENCES

Abtahi, A.A., 1985. "Aspect ratio effects on wings at low reynolds number". PhD Thesis in Aeroespace and Ocean Engineering, Faculty of the Virginia Polytechnic Institute and State University, Blacksburg, Virginia.

Ananda, G., Sukumar, P. and Selig, M., 2012. "Low-to-moderate aspect ratio wings tested at low reynolds numbers". *In*: *Proceedings* of the 30TH AIAA APPLIED AERODYNAMICS CONFERENCE. doi:10.2514/6.2012-3026.

Anderson, J., 2010. *Fundamentals of aerodynamics*. McGraw-Hill Education, New York.

Bastedo, W.G. and Mueller, T.J., 1986. "Spanwise variation of laminar separation bubbles on wings at low reynolds number". *Journal of Aircraft*, Vol. 23, No. 9, pp. 687–694. doi:10.2514/3.45363.

Bourdin, P., 2002. "Numerical predictions of wing-tip effects on lift-induced drag". *In*: *Proceedings* of the 23RD CONGRESS OF ICAS.

Celik, I., Ghia, U., Roache, P., Freitas, C., Coloman, H. and Raad, P., 2008. "Procedure of estimation and reporting of uncertainty due to discretization in cfd applications". *Journal of Fluids Engeneering*, Vol. 130, No. 7, pp. 078001–1–4. doi:10.1115/1.2960953.

Cummings, R., Giles, M. and Shrinivas, G., 1996. "Analysis of the elements of drag in three-dimensional viscous and inviscid flows". *In*: *Proceedings* of the 14TH AIAA APPLIED AERODYNAMICS CONFERENCE. doi: 10.2514/6.1996-2482.

Maughmer, M.D., 2006. "The design of winglets for low-speed aircraft". *Technical Soaring*, Vol. 30, No. 3, pp. 61–73.

McCormick, B.W., 1995. *Aerodynamics aeronautics and flight mechanics*. John Wiley & Sons, United States, 2nd edition.

Monsch, S., Figliola, R., Thompson, E. and Camberos, J., 2007. "Computation of induced drag for 3d wing with volume integral (trefftz plane) technique". *In*: *Proceedings* of the 45TH AIAA AEROSPACE SCIENCES MEETING AND EXHIBIT. doi:10.2514/6.2007-1079.

Raymer, D.P., 2018. *Aircraft design*. American Institute of Aeronautics and Astronautics Inc., United States of America, 6th edition.

Roache, P.J., 1997. "Quantification of uncertainty in computational fluid dynamics". *Annual Review of Fluid Mechanics*, Vol. 29, No. 1, pp. 123–160. doi:10.1146/annurev.fluid.29.1.123.

Roberts, S.C., 1966. *U. S. Army aviation maieriel laboratories technical report 65-79*. Mississippi State University, United States of America.

Spalart, P. and Rumsey, C., 2007. "Effective inflow conditions for turbulence models in aerodynamic calculations". *Aiaa Journal*, Vol. 45, pp. 2544–2553. doi:10.2514/1.29373.

Tumelero, B., da Silva, F.D. and Cuenca, R.G., 2021. "Estudo de metodologia para dimensionamento de endplates em aeronaves de baixas velocidades". *In*: *Proceedings* of the XVII Congresso Nacional de Estudantes de Engenharia Mecânica. doi:10.26678/ABCM.CREEM2020.CRE2020-0124.

Tumelero, B., da Silva, F.D. and Cuenca, R.G., 2022. "Comparison of different modeling strategies for the prediction of lift and drag of an uav wing". *In*: *Proceedings* of the 2022 Escola de primavera de transição e turbulência. doi: 10.26678/ABCM.EPTT2022.EPT22-0017.

Van der Vooren, J. and Slooff, J., 1994. *CFD-based drag prediction*. Royal Netherlands Aerospace Centre, Netherlands.

Wilcox, D.C., 2006. *Turbulence modelling for cfd*. DCW Industries, La Cañada, 3rd edition.

6. RESPONSIBILITY NOTICE

The authors are solely responsible for the printed material included in this paper.